Title: Spatial point pattern analysis identifies mechanisms shaping the skin parasite landscape in *Leishmania donovani* infection

Authors

Johannes S. P. Doehl[1¶], Helen Ashwin[1], Najmeeyah Brown[1], Audrey Romano[1#], Samuel Carmichael[2], Jon W. Pitchford[2], Paul M. Kaye[1*]

Affiliations

[1] York Biomedical Research Institute, Hull York Medical School, University of York, York, YO10 5DD, UK

[2] Departments of Biology and Mathematics, University of York, York YO10 5YW, UK.

[¶] Current address: Vector Molecular Biology Unit, Laboratory of Malaria and Vector Research, National Institute of Allergy and Infectious Diseases, National Institutes of Health, 12735 Twinbrook Parkway, Rockville, MD 20852, USA

[#] Current address: BILHI Genetics, 60 Avenue André Roussin, 13016, Marseille, France

* Correspondence to: P.M.K. (email: paul.kaye@york.ac.uk)

Abstract

Increasing evidence suggests that infectiousness of hosts carrying parasites of the *Leishmania donovani* complex, the causative agents of visceral leishmaniasis, is linked to parasite repositories in the host skin. This is particularly true for asymptomatic to moderately symptomatic hosts with no or minimally detectable parasitemia. However, a detailed description of the dispersal and dispersion of parasites and parasitized host phagocytes in the skin is still lacking. Here, we combined image analysis with spatial point pattern models borrowed from ecology, providing a new route to predicting modes of skin parasite dispersal and characterizing their dispersion. Our results suggest that, after initial parasite seeding in the skin, parasites form self-propagating networks of parasite patch clusters in the skin that may contribute to parasite outward transmission. This combination of imaging and ecological pattern analysis to identify mechanisms driving the skin parasite landscape offers new perspectives on parasitism by *Leishmania donovani* and may also be applicable to elucidating the behavior of other intracellular tissue-resident pathogens.

Introduction

Vector-borne kinetoplastid parasites of the *Leishmania donovani* complex are the causative agents of zoonotic and anthroponotic visceral leishmaniasis (VL). *Leishmania* parasites occur in two distinct stages; as extracellular promastigotes in their insect vector, hematophagous phlebotomine sand flies (Diptera: Psychodidae: Phlebotominae)[1], and as intracellular amastigotes in the mammalian host[2]. VL is associated with 3.3 million disability-adjusted life years (DALYs)[3] and 20,000-40,000 annual deaths in 56 affected countries[4]. There is no available prophylactic vaccine[5] and available drugs are either expensive and/or show significant toxicity[6].

Infection of a naïve host with *Leishmania* parasites occurs through the bite of infected sand flies into the skin, the only interface between insect vector and host. *L. donovani* disseminate from the skin to deeper tissues including the spleen, liver and bone marrow causing systemic pathology, but the skin is commonly asymptomatic[7]. Blood parasite load (parasitemia) is considered the main determinant of outward transmission potential and as a surrogate measure of host infectiousness in VL[8]. In a recent study[9], the infectiousness of *L. donovani*-infected patients in India as measured by xenodiagnoses was found to positively correlate with spleen parasite load as well as blood parasitemia determined by qPCR, with increasing odds of being infectious above 101 genome copies per ml of blood. Of note, out of 7 infectious patients that remained infectious after drug treatment, 6 had no detectable blood parasitemia[9]. We previously demonstrated in the VL pathology-free C57BL/6 CD45.1. *Rag*$^{-/-}$ (herein referred to as RAG) mouse model that despite high parasite burden in deep tissues, parasitemia was comparatively low (2,000 – 2,500 parasites / ml blood or equivalent to ~2 – 3 amastigotes / blood meal) and did not correlate with outward transmission success[10].

Collectively, these data, together with other studies in the hamster model of VL[11], in canine VL[12] and in human post-kala azar dermal leishmaniasis[9, 13, 14] support the need to consider skin parasite load as a potential contributor to infectiousness across the disease spectrum attributable to the *L. donovani* complex.

A confounding feature associated with sampling in many studies of host infectiousness related to skin parasite residence is the possibility of spatial heterogeneity in parasite distribution. We recently demonstrated that *L. donovani* accumulate in patches in asymptomatic host skin, where their dispersion is a strong predictor for the infectiousness of an asymptomatic host[10]. However, a detailed characterization of the micro- and macro-scale dispersion of *Leishmania* parasites (and de facto, parasitized host cells) in the skin is lacking. Also, a more detailed understanding the mechanisms of skin parasite dispersal would provide insight into a poorly understood aspect of the *Leishmania*-host interaction and that, in the longer term, might lead to the development of interventions to limit landscape complexity and hence reduce host infectiousness.

Here, we describe in detail the micro- and macro-scale dispersion of tandem-dimer Tomato (tdTom) *L. donovani* parasites in the skin of 23 long-term infected RAG mice. We used image analysis tools to extract data from whole skin images and microscopy images of punch-biopsy skin sections. We adopted spatial point pattern methodologies commonly applied in ecology and other fields to interrogate skin parasite dispersion in silico and to make predictions about modes of dispersal[15]. Our results suggest that skin parasite patches form “clusters” with a larger patch at the cluster center and smaller patches around them. These clusters may form as a result of reseeding *L. donovani* amastigotes from a larger patch within a locally varying

radius around it. Our data therefore suggest that after an initial parasite seeding event in the skin from the circulation, skin parasite patches are the main driver of their own dispersal. This process would also serve to enhance skin parasite patch growth, as larger patches consist of a merger of smaller patches. This study provides new insights into the complex mechanisms underlying *L. donovani* dispersal and dispersion in the skin and exemplifies an approach that may help understand dispersal and dispersion of phylogenetically diverse intracellular pathogens in the skin and other tissues.

Results

Parasites accumulate in phagocytic cells in the reticular dermis

We generated confocal images of 20 µm thick longitudinal skin biopsy sections from four different RAG mice (RAG19-22). Visual image inspection suggested that *L. donovani* amastigotes resided primarily in the dermis (**Fig. 1A**). For confirmation, two distinct approaches were used. We calculated the shortest distance measurements of individual amastigotes to the epidermis (**Fig. 1B**) and conducted computationally aided amastigote counting in each skin layer (**Fig. 1C**). The former showed that the majority of parasites resided in the reticular dermis, which comprises the deeper 90% of the dermis[16]. The latter approach showed that the dermis harbored on average ~36x and ~9x more amastigotes / mm^2 than the epidermis and hypodermis, respectively.

Leishmania amastigotes are obligatorily intracellular parasites, residing in phagocytic cells. Not surprisingly, therefore, infected host cells were also found predominantly in the dermis (~29x and ~26x more frequent than in epidermis and hypodermis, respectively; **Fig. 1D**). Thus, parasite dispersion was reflected in host cell dispersion. In fact, the number of parasites / mm^2 skin correlated very strongly with the number of infected cells / mm^2 (Spearman r: $P<0.0001$, $r=0.9364$, 95% CI: 0.8432 – 0.9749; **Fig. 1E**), suggesting that the proportion of infected cells increased with the increase in parasite burden.

In the skin, macrophages and dendritic cells (DCs) are the most abundant phagocytic cell populations in steady state[17]. It has previously been shown that alternatively activated tissue-resident macrophages (TRM2s) expressing the mannose receptor (Man^R) are a preferred host for *L. major* in the mammalian skin[18]. CD11c is a generic DC marker[19], although it can

be expressed by tissue macrophages under inflammatory conditions[20]. Thus, Man^{R} and CD11c were used to detect TRM2s and DCs, respectively. We observed that 42% (95% CI: 31% - 52.7%) and 7% (95% CI: 4.7% - 9.3%) of all infected cells were Man^{R+} and $CD11c^{+}$, respectively (**Fig. 1F**). Thus, while Man^{R+} TRM2s also appear to be permissive host cells for *L. donovani* amastigotes, ~51% of all infected cells detected were neither Man^{R+} or $CD11c^{+}$. Further, of all Man^{R+} and $CD11c^{+}$ cells, 19.1% (95% CI: 12.6% - 25.7%) and 9.8% (95% CI: 5.5% - 14.1%) were infected, respectively (**Fig. 1G**), leaving a large proportion of these cells uninfected (~80.9% and ~90.2% of all Man^{R+} and $CD11c^{+}$ cells, respectively). These data suggest that the observed diverse cellular tropism is not due to saturation of permissive targets such as TRM2s.

Skin parasite patch landscape is sculpted by parasite reseeding and growth

Whole body skins from 23 untreated, tdTom-*L. donovani* long-term infected (6-7 months) RAG mice (Rag1 – 23) were used to analyze the dispersion of skin parasites. These RAG mice had been used as control mice in seven independent experiments (Exp 1 – 7) and were comparably treated (**Fig. S1A & B**). We used qPCR-based parasite kDNA detection in multiple skin biopsies from each RAG mouse matched against a standard curve to estimate parasite burden per skin biopsy. Comparing parasite burden from biopsies across the skin of each mouse established whether skin parasite burdens varied geographically across the mouse skin and between mice and the mean parasite burden per biopsy per mouse (**Fig. 2A & S2A**). We found considerable variability in mean parasite burden between RAG mice (Kruskal-Wallis Test: $H = 315.7$, $df = 22$, $P<0.0001$) and in parasite loads between biopsies from the same RAG mouse (**Fig. S2A**) which suggested a heterogeneous parasite dispersion in the host skin, as expected from our previous study[10]. Further, data on the parasite burden

per biopsy showed in most cases a departure from a normal distribution for each RAG mouse (Shapiro-Wilks test: see **Table S1**) and a lack of equal variance (Brown-Forsythe test: F (DFn, DFd) = 2.928 (22, 409), P<0.0001). Thus, the median parasite burden per biopsy was used to estimate the total parasite burden in skin for each RAG mouse. In turn, this was used to estimate the mean parasite burden per cm^2 of skin (**Table S1**). Despite intravenous inoculation of equivalent numbers of parasites, there was considerable variability in total parasite burden in skin between RAG mice, ranging from ~$1x10^6$ (RAG12) to $1.24x10^9$ (RAG3) parasites per mouse (**Table S1**).

Akin to parasite loads, skin parasite patch counts were also highly variable between RAG mice, ranging from ~1.2 patches per cm^2 (Rag14) to ~32.9 patches per cm^2 (Rag8) and 76 (RAG14) to 2,457 (RAG10) patches per mouse (**Fig. 2B & Table S1**). We also measured the area of skin parasite patches. Patches measured ~0.00004 cm^2 (50x smaller than a 25G needle prick) to 53 cm^2 (>80% of the mouse skin; **Fig. 2C, D, S3 & Table S1**). Most patches were small (<0.1 mm^2) and only few were large (>1mm^2), resulting in a heavily skewed dataset (**Fig. S2B**). More precisely, ~84% detected patches were 0.004 mm^2 – 0.099 mm^2 but accounted for merely ~12.7% of the total patch area (**Fig. 2E**). Conversely, only ~3.3% of detected patches were >1 mm^2 but accounted for ~64% of the total patch area. In an individual mouse, these proportions were even more extreme (**Fig. S4**). In fact, there was a strong correlation between the total patch area and the largest patch in any given mouse (Spearman r: p<0.0001, r=0.9792, 95% CI=0.9496 – 0.9915; **Fig. 3A**). Interestingly, we identified no preferred site of skin parasite patch accumulation, suggesting that skin parasite patch dispersion may be random. However, when we plotted skin parasite patches by size category, we observed that mid- (red and blue symbols; 0.01 – 1 cm^2) and large-range (violet

and green symbols; ≥1 cm^2) skin parasite patches were usually surrounded by several small patches (**Fig. 2F & S5**). Moreover, when focusing on mid-range skin parasite patch dispersion, these patches appeared to follow unidentified tracks across the skin in several RAG mice (**Fig. S5**). These observations suggested that, while skin parasite patch dispersion may look different between RAG mice, dispersal is not a random process, but governed by unknown factors in the skin. Our subsequent analysis aimed to test this assertion.

We observed that skin parasite patches had higher tdTomato signal at their center compared to their periphery. Since tdTomato amastigotes are approximately of equal brightness, it is reasonable to suggest that the brighter signal at the patch center correlated to higher amastigote density. A grey-scale pixel analysis in the red channel to measure tdTomato signal intensity per pixel (**Fig. 2H & S6**) showed that most mean grey-scale values per patch were close to the cutoff of 70 (**Fig. 2G, Fig. S2C**). However, when patch area was correlated with their respective average grey-scale value, it showed a strong correlation (**Fig. 3B**; Spearman r: $P<0.0001$, $r=0.6554$, 95% CI=0.6476 – 0.6631). This suggested that as patches grew outward, they became more densely populated with amastigotes. Cross section analysis of tdTomato signal intensity in selected parasite patches showed volcano-like graphs with steep shoulders, suggesting that the amastigote bulk is concentrated at the center of a patch and then thins out quickly at the patch periphery (**Fig. 2I & J**).

We also observed that larger patches contained multiple areas of high tdTomato-signal (**Fig. S6**). Correlating patch area and density peaks per patch suggested that all mid-range and larger patches had multiple density peaks (Spearman r: $P<0.0001$, $r=0.3831$, 95% CI=0.3714 – 0.3947; **Fig. 3C**). The statistically weak correlation was explained by the broad base of

small patches with only one or two peaks. Accumulation of density peaks per patch only became apparent when patch areas exceeded 1 mm^2 (>10^6 μm^2). This suggested that smaller expanding patches grew into one another to form bigger patches. Further, large patches indicated areas where initial parasite seeding had been higher and / or earlier than in other areas of the skins. Conversely, patch growth may have been faster in areas where large patches occurred.

Further, we investigated the relationships between mean parasite burden / cm^2, parasite patch counts / cm^2 and total patch area / cm^2 by correlation plot analysis. Mean parasite burden / cm^2 correlated strongly with total patch area / cm^2 of skin, suggesting that increases in total skin parasite burden would also increase total parasite patch area and thus may be the driver of skin parasite patch growth (**Fig. 3D**; Spearman r: P<0.0001, r=0.7589, 95% CI=0.4948 – 0.8947). Parasite patch counts / cm^2 correlated only moderately with parasite burden / biopsy (**Fig. 3E**; Spearman r: P=0.0021, r=0.5741, 95% CI=0.1997 – 0.8022), suggesting that increases in skin parasite burden was more closely related to patch expansion than new patch seeding. Conversely, when total patch area / cm^2 was correlated with the patch count / cm^2, it showed a very strong positive correlation (**Fig. 3F**; Spearman r: P<0.0001, r=0.8656, 95% CI: 0.6984 – 0.9432), suggesting that the proportion of parasitized host skin is largely determined by the number of observed patches. Correlating the median of patch areas per skin for each RAG mouse to the total patch counts per skin, we found a moderately negative correlation (**Fig. 3G**; Spearman r: P=0.006, r=-0.5148, 95% CI=-0.7701 to -0.1175), which suggested that the more patches a RAG mouse skin had the more of these patches were likely to be small (<0.1 mm^2).

While data skewness is an underlying characteristic of skin parasite dispersion for any given sample, skewness cannot be directly inferred onto a population. To test whether the observed sample skewness was a general population feature, we divided by the standard error of skewness (SES)[21]. The resulting test statistic being outside the interval [-2, 2] infers that data skewness was a population property (**Table S1**). For instance, total patch area per skin was very strongly correlated with the degree of skewness in the patch area data (**Fig. 3H**; Spearman r: P<0.0001, r=0.8686, 95% CI=0.7044 – 0.9445), suggesting that as parasite patchiness increased in the skin, mid-range patches give way to a few large patches surrounded by many small patches. This appears to be a common population feature, given the correlation of the test statistic to the total patch area / skin was even stronger than compared to the sample skewness (**Fig. 3I**; Spearman r: P<0.0001, r=0.9279, 95% CI=0.8311 – 0.9701).

The skin parasite patch landscape is heterogeneously clustered

We previously established that skin parasite dispersion pertained to concepts of landscape epidemiology[10]. Thus, we applied methodologies of spatial point pattern analysis commonly used in landscape epidemiology to characterize the skin parasite dispersion further to find potential modes of parasite dispersal in host skin[15]. We converted our skin parasite patch data into spatial point patterns by mapping the center of mass of each patch to a window characterized by the respective RAG skin outline (**Fig. 4A, Fig. S7, Table S2**). After verifying the absence of point duplications, characteristics of skin parasite patches (e.g. area and density) could optionally be reintroduced to the pattern as a mark (**Fig. 4B, Fig. S8**). Focusing on patch area, we calculated the intensity of point distributions (equivalent to dispersion) with or without a mark and graphically represented the measured point pattern intensities (**Fig. 4C,**

D, S9 & S10). Alternatively, we calculated the intensity per cm^2, which is akin to the number of patches per cm^2 and found that both methods corroborated one another (**Table S1 & S2**). As shown in **Figure 4C** (without area mark), intensity showed the distribution of patches by center of mass location, whereas in **Figure 4D** (with area mark) intensity showed the distribution of patches by size in the skin (see also **Fig. S9 & S10**). Both intensities showed a clear departure from a homogeneous distribution.

To gain further understanding of how patches related to one another, we performed a cluster analysis, choosing 3.9 mm as the maximum distance between patch borders (see Methods for justification). This analysis showed small patches clustering strongly around larger patches (**Fig. 4E & S11**), which confirmed our previous observation from **Figure 2F** (see also **Fig. S5**). Further, this analysis showed the formation of networks of closely clustered patches, which may enhance the likelihood of parasite pick up by a biting sand fly without having to densely parasitize the whole skin (**Fig. 4E & S11**).

These observations suggested that skin parasite patch dispersion is likely to be neither homogeneous nor random. To formally test for homogeneity of parasite patch distributions, a quadrat test based on the Fisher's exact test was applied, which rejected homogeneity for all skin parasite patch distributions (P=0.001; **Table S2**). Thus, an inhomogeneous Poisson point process (IPP) was used as a null hypothesis. Analogue to a homogeneous Poisson point process, an IPP is assumed to be correlation-stationary (the pair correlation between two spots in the window depends only on their relative positions) and isotropic (the distribution is unaffected by the pattern orientation). However, isotropism was rejected for about half of all skin parasite patch patterns (**Fig. 4F & S12**); RAG14 did not produce a reliable test result due

to its sparse number of parasite patches. To assess correlation-stationary, we split the point patterns into two portions of equal numbers of observations and applied the inhomogeneous K-function, which is derived from Ripley's K-function, to each half of the pattern. The analysis showed considerable disagreement between the two plots for several mice indicating that the whole point pattern was not correlation-stationary (**Fig. S13**). In addition, the inhomogeneous K-function showed considerable disagreement between different applied boarder corrections, which suggested that an IPP was a bad fit to describe skin parasite patch patterns. In addition, we rejected a Poisson distribution for our skin parasite patch patterns based on a Quadrat Count test (**Table S2**). These disagreements suggested that the spatial scale of point interactions, which is assumed to be constant by the inhomogeneous K-function[15], was locally variable for our skin parasite patch patterns. Thus, by assuming a point process that was locally stationary and isotropic, but showed a varying rescaling factor between locations in the skin, we could use a locally scaled K-function to rerun the correlation-stationary test. Although not perfect, agreement between the two plots per mouse and between different boarder corrections was significantly improved (**Fig. 4G & S14**), suggesting that parasite patch distribution was locally scaled.

We proceeded with the scaled L-function, derived from Besag's L-function, to determine if skin parasite patches were evenly spaced (regular), randomly spaced (independent) or clustered (**Fig. 4H & S15**). While the fitted data (black solid line) generally departed from the hypothetical random distribution toward a clustered one (black solid line above dotted red line), only RAG11, RAG13, RAG14 and RAG23 showed a clear departure from the global simulation envelops of a hypothetical random distribution (grey shaded area) toward clustering. To confirm these results, we used the pair correlation function (PCF), which is not

cumulative in nature and only contains contributions of interpoint distances ≤ r. The scaled PCF analysis showed for most mice, parasite patch patterns departed from the theoretical random distribution (dotted red line) toward a clustered point process (black line above the red dotted line), in particular, at short distances between patches (**Fig. 4J & S16**). With increased interdistances between patches, some skin parasite point patterns showed an approximation to more point independence. Applying the K- and nearest-neighbor (G-) function to the point pattern residuals showed a clear departure of independence toward clustering at shorter interdistance, indicating positive point dependence (black line outside the upper confidence intervals [dotted green line]) for both tests (**Fig. 4K, L, S17 & S18**).

Modelling the point process behind skin parasite patch patterns suggests influence of covariates

Consequently, to model skin parasite patch distribution we adopted a model that accounted for positive point (patch) dependence (clustering) and was tolerant to a locally varying distribution scale. We used different cluster processes (Cauchy, Matérn, Thomas and Variance-Gamma cluster processes) as described by a Baddeley et al. ('spatstat'[15]) that assume that cluster formation is based on a parental point distribution that seeded the observed points around themselves within a radius, which is variable between clusters due to the locally scaled nature of cluster distribution. This assumption is reflected in our data showing that small skin parasite patches cluster around mid-range and large patches (**Fig. 2F, 4E, S5 & S11**).

In the absence of any measured covariates, we used the Cartesian coordinates of each patch's center of mass as covariates in the model to observe potential local trends. The best

model was then selected by a stepwise elimination of covariates by the application of the Akaike Information Criterion (AIC). Most fitted point patterns performed best without the x- and y-coordinate covariates, except for RAG4, RAG21 and RAG23 (reliant on the y-coordinate) and RAG17 (reliant on the x-coordinate; **Table S3**). Further, 13 of the 23 skin parasite patch distributions were best fitted by a Matérn cluster process, while the other 10 were best fitted by a Thomas cluster process. The Matérn cluster process assumes a uniform distribution of offspring around the parental point, while the Thomas cluster process assumes offspring to be randomly displaced from the parental point[15]. Checking the parameters selected by the model showed that they were within a reasonable range, confirming model validity (**Table S4**). This was further confirmed by the scaled L-function of the selected fitted models for each skin parasite patch pattern (**Fig. 5A & S19**). The L-functions of the fitted models resembled closely the L-functions from the point pattern analyses above (**Fig. 4H & S15**). Further, we used the selected fitted models to run 4 simulations each to see if the outcome would resemble the distributions the original data (**Fig. 5B & S20**). With a few exceptions, like RAG3, the simulation outputs provided a good representation of the original skin parasite patch dispersion data (**Fig. 4A & S7**).

Based on these findings, we can deduce how skin parasite dispersal may operate. The Matérn and Thomas cluster processes assume points of origin that seed new points within a set radius clustering around them to create an observed clustered point dispersion. In a locally scaled setting, as it is the case for our skin parasite patch distribution, this radius is locally varying in length and thus distinct for each patch cluster. Analogous, after an initial parasite seeding events in the host skin, skin parasite patch dispersal may be explained by existing patches locally seeding new patches around themselves, while growing outward,

creating a self-propagating network of skin parasite patch clusters in the host skin (**Fig. 6 & S21**).

Discussion

We have previously shown that having skin parasites distributed into patches provides a mechanism to enhance host infectiousness to sand fly vectors[10]. However, the underlying mechanisms involved in skin parasite patch formation remain elusive. Here, we used spatial point pattern methodologies to gain insides into these mechanisms of skin parasite dispersal by selecting models that can describe observed skin parasite patch dispersion. To our knowledge, this is the first study to make use of spatial point pattern methodologies[15] in this way. The Matérn and Thomas cluster processes, which were identified to best describe how the observed skin parasite patch dispersion occurred, both assume points of origin which seed new points within, in our case, locally varying radii clustering around them. During experimental VL in this immunodeficient setting, we, therefore, propose that existing skin parasite patches locally seed new patches around themselves, giving rise to patch clusters with a central large patch.

In vivo, *Leishmania* amastigotes reside in phagocytic cells in the host dermis, primarily macrophages[21]. Therefore, parasite dispersion is linked to the phagocytic host cell dispersion a subject on which scant information is available. In the steady-state dermis, macrophages and DCs are the primary phagocytic cell populations[17]. Interestingly, macrophages and DCs have very particular distributions in steady-state skin. Branched DCs are predominantly interstitially localized right underneath the dermal-epidermal junction[22, 23]. Macrophages are commonly found underneath these DCs; mostly interstitially. Deeper in the reticular dermis, both cell types associate perivascular to blood vessels rather than lymphatic vessels and DCs at this site are more rounded. Among the different macrophage populations in the skin, it was shown that Man^{R+} TRM2s play an important role as long-term *L. major* host cells[18]. In

356 addition, the rate of parasite infection in Man^{R+} TRM2s (~45%) correlated strongly with the
357 severity of skin pathology and parasite survival in the host. The rate of infection in DCs was
358 much lower (22.5%), indicating a preference of *L. major* for Man^{R+} TRM2s[18]. In our study, the
359 observed infection rates for both cell types with *L. donovani* were less than half of this
360 (~19.1% and 9.8%, respectively), but *L. donovani* similarly showed a preference for Man^{R+}
361 TRM2s over DCs (5:1). These cells constituted almost 50% of all infected host cells.
362 Conversely, 50% of host cells belonged to neither group; presumably, other phagocyte
363 populations[21]. Interestingly, the majority of Man^{R+} TRM2s and CD11c^{+} DCs (~80.9% and
364 ~90.2%, respectively) were uninfected in the analyzed skin sections, despite the high number
365 of parasites present in some of the sections. This raised the question why the small
366 proportion of infected host cells should be clustered close together and also indicates that
367 cellular tropism observed is not due to saturation of preferred targets.
368
369 Further, our analysis suggested that the process of skin parasite patch formation may be
370 influenced by yet to be identified covariates. One covariate may be proximity to blood vessels
371 as Man^{R+} TRM2s often colocalize to them in the dermis, where they can pick up
372 macromolecules from the blood[18, 24]. This could explain why mid-range patch distribution
373 appeared to follow unidentified lines in the skin and why there was no preferred location for
374 parasite accumulation in the skin. Further, proximity to blood vessels may also enhance
375 access to nutrients from the circulation for parasitized phagocytic cells and thus, indirectly
376 promote parasite proliferation. Also, parasite proximity to blood vessels would improve their
377 chances to be found by a probing sand fly. Future analysis could potentially confirm blood
378 vessel association of parasite patches by proximity measurements. However, three-
379 dimensional (e.g. light sheet) microscopic imaging data would be needed to achieve this.

380

381 Our data also indicate that the accumulation of infected host cells into patches could be
382 analogous to a granulomatous response that induces host cell migration to infection sites in
383 the skin. This may be akin to what is observed early in the process of *L. donovani*-dependent
384 granuloma formation in the liver, where Kupffer cell migration toward a granuloma-initiating
385 infected Kupffer cell results in a heterogeneous Kupffer cell distribution and condensation of
386 infected Kupffer cells at the core of the granuloma[25, 26]. The lack of an adaptive immune
387 response in our RAG mouse model of skin infection provides a unique window on innate
388 macrophage aggregation into a type of innate granuloma, as demonstrated in response to
389 *Mycobacterium marinum* infection in young zebrafish embryos[27].

390

391 It remains to be determined whether skin parasite patches form because infected host cells
392 are attracted to these locations in the dermis, or if these locations stimulate parasite growth.
393 Our data suggested that new skin parasite patches may primarily be seeded from existing
394 patches. We observed that larger patches were surrounded by smaller patches that emerged
395 within limited distances from the larger patches, resulting in patch clustering. If, akin to
396 parasite dispersion, parasite dispersal is also linked to its host cells, then, mechanistically,
397 skin parasite patch clustering could occur by escape of infected host cells from these “innate
398 granuloma”-like parasite patches as was demonstrated in *M. marinum*-infected zebrafish
399 embryos[28]. Conversely, parasites could be redistributed to uninfected host cells within a
400 limited radius from patches by amastigote release from ruptured host cells or by intercellular
401 passage. Macrophages are known to form a variety of open-ended tunneling nanotubes
402 (TNT) between one another at a distance and such structures have been implicated in the

spread of several respiratory viruses and HIV-1[29, 30, 31]. We know of no formal evidence, however, to show that *Leishmania* parasites are transported between macrophages via TNTs.

The cores of patches are very dense with parasites / heavily infected host cells, but the patch fringes are much less heavily parasitized suggesting that parasites proliferating strongly within a patch are then pushed outward. Mandell & Beverley (2017) observed that not all amastigotes in the host skin proliferate at the same rate and described two distinct amastigote populations; one that was dormant, the other proliferative[32]. Thus, skin parasite patches may represent areas of where amastigotes are proliferative, while inter-patch space could mark areas of dormant amastigotes. Whether host cell metabolism stimulates / supports amastigotes to proliferate in the mammalian host skin[33] remains to be determined.

While skin parasite dispersion and dispersal may not significantly influence sand fly infectiousness[34], they do govern mammalian host infectiousness and affect parasite prevalence in a sand fly population[10]. The results of the new analysis presented here advance our knowledge of this process in two major ways. First, we provide new insights into how the resulting network of clustering skin parasite patches may enhance outward transmission probability. Considering the size of a sand fly (length: 2-3 mm), if skin parasite patches cluster closer than 4 mm together, then no matter where and in what orientation a sand fly lands on a host skin, there is a great likelihood of a patch being in biting range (**Fig. S1D**). Since skin parasite patches are densely parasitized, these patch networks would increase the chance of high parasite loads being acquired by a sand fly and eliminate the need for parasitism of the entire skin. Second, our model provides a framework for future studies aimed at identifying the mechanisms behind parasite and phagocyte dispersion in this setting of

427 immunodeficiency and in a lymphocyte-replete environment. Such studies may open new
428 therapeutic opportunities for manipulating the complexity of the parasite skin landscape
429 during infection, with the aim of reducing host infectiousness.

Materials and Methods

Ethics statement

All animal usage was approved by the University of York Animal Welfare and Ethics Review Committee and the Ethics Review Committee at FERA Science Ltd., and performed under UK Home Office license ('Immunity and Immunopathology of Leishmaniasis' Ref # PPL 60/4377).

Mouse, Leishmania and sand fly lines

C57BL/6 CD45.1.*Rag2*$^{-/-}$ (RAG) mice (originally obtained from the National Institute of Medical Research, London, UK) were used in this study. All animals were bred and maintained at the University of York according to UK Home Office guidelines. The Ethiopian *Leishmania (Leishmania) donovani* strain (MHOM/ET/1967/HU3) had been transfected with a tdTom gene[35] to generate a tdTom-*L. donovani* line in another study[26]. The parasites were maintained RAG mice by repeat-passage of amastigotes. For both parasite passage and RAG mouse infection, tdTom-*L. donovani* amastigotes were isolated from the spleens of long-term infected RAG mice and i.v. at $8x10^7$ amastigotes / uninfected RAG mouse as previously described[10].

Mouse skin harvest

All animals used in this study were untreated control animals pooled from 7 different experiments. All animals were exposed to comparable experimental conditions (**Fig. S1A & B**). Mouse skin harvest was performed as previously described[10]. Briefly, RAG mice were sacrificed in a CO_2-chamber, followed by cervical dislocation. Animals were first shaven with electric clippers and then treated with a depilation cream (Veet) for up to 3 min. The depilation

cream was scraped off and residual cream was washed off under running water. Mice were skinned by an abdominal double-Y incision, removal of ears and exclusion of paws and tail (**Fig. S1C**). The skin was pulled from the rump over the head and then cut off at eye-level. Excess adipose tissue was removed with curved tweezers and skins were kept in complete RPMI on ice until stereomicroscopic imaging and subsequent biopsy punching.

Genomic DNA extraction

16 or 24 skin biopsies (ø 0.6 cm) were taken from each skin as previously described[10]. All genomic DNA (gDNA) extractions were performed with either the DNeasy® Blood & Tissue spinning column kit (Qiagen) or the DNeasy® 96 Blood & Tissue plate kit (Qiagen) according to supplier's protocol.

Quantitative Polymerase Chain Reaction

All quantitative real-time PCRs (qPCR) were performed as previously described[10]. Briefly, previously characterized *Leishmania*-specific kinetoplastid DNA primers (Accession number AF103738)[36] were used at a final concentration of 200 nM. 2 ng of total gDNA extracted from skin biopsies were used / reaction. Fast SYBR® Green Master Mix (Applied Biosystems) was used according to supplier's guidelines. Reactions were run in a StepOnePlus™ thermal cycler (Applied Biosystems) with a thermal cycle of 95°C for 20 s, a cycling stage of 40 cycles of 95°C for 3 s, 60°C for 5 s, 72°C for 20 s, 76.5°C for 10 s (data read at final step), followed by the standard melt curve stage. Data was analyzed by StepOne™ Software v.2.3.

Microscopy

Fluorescent stereomicroscopy of whole skins was performed as previously described[10]. Briefly, a series of 30-40 images at 12x magnification were taken / skin to image the whole skin area from the hypodermal face. All images were taken under the same conditions. Image-series were collated in Adobe® Photoshop® to render a single image of the whole mouse skin.

For confocal microscopy, fixation and cryo-preservation of skin punch biopsies (ø 0.6 cm) was adapted from Accart et al. (2014) to optimize tdTomato-signal and skin integrity preservation after skin freezing and cutting[37]. Briefly, skin biopsies were fixed in 2% Formaldehyde in PBS for 15 min at room temperature (RT), rinsed 3x in 15% Sucrose/PBS and incubated overnight at 4°C in a Tris-Zinc fixative (per 100 ml: 1,211.4 mg Tris-base, 501.5 mg $ZnCl_2$, 500.5 mg Zinc Acetate Dihydrate, 50.6 mg $CaCL_2$, 15 g Sucrose dissolved in dH_2O) on a shaker. The next day, biopsies were rinsed 3x in 15% Sucrose/PBS and incubated in 7.5% Porcine Gelatine (300 bloom) in 15% Sucrose/PBS in individual cryo-molds at 37°C for 1 h. Biopsies were sealed upright in the gelatine blocks by congealing at RT. Gelatine/specimen-blocks were cut down in size, flash-frozen in isopentane on dry ice, further frozen in OCT in a cryo-mold on dry ice and stored at -80°C. Frozen skin biopsies were longitudinally cut at 20 µm thickness to expose all skin layers and section were placed on superfrosted microscopy glass slides. Gelatine was removed by slide incubation in PBS at 37°C for up to 30 min.

Antibody-labelling of skin sections was adapted from Dalton et al. (2010)[38]. Briefly, slides were rinsed in PBS, permeabilized for 15 min with 0.3% Triton X-100/PBS (perm. buffer),

rinsed in PBS, blocked for 30 min with Image-iT™ FX Signal-enhancer (Invitrogen), rinsed with PBS and further blocked for 30 min with 5% serum + FcBlock (1:1000) in perm. buffer. Primary antibodies were diluted in 5% BSA in perm. buffer (CK-10 [1 µg/ml] (Abcam: ab76318), Mannose Receptor [1 µg/ml] (Abcam: ab64693), CD11c [5 µg/ml] (Abcam: ab33483)) and incubated with specimen for 90-120 min at RT. Slides were washed 3 times in 0.5% BSA/PBS. Secondary antibodies were diluted in 5% BSA in perm. buffer (BV421 [1 µg/ml] [Biolegend: 406410]; Alexa Fluor 647 [Invitrogen: A-21451]) and incubated for at least 60 min at RT. Slides were washed 2 times in 0.5% BSA/PBS and once in PBS at RT. Specimen were counterstained with 0.2 µM YOYO-1 in PBS for 30 min at RT and washed 2 times in PBS. Slides were mounted in ProLong Gold (ThermoFisher Scientific) and left overnight at 4°C. Slides were sealed the next day and imaged with a 40x oil-immersion objective (400x magnification) on a fully motorized invert LSM 880 confocal microscope with Airyscan (Zeiss) by z-stacked tile-scanning.

Stereomicroscopic image analysis (macro-scale)

All whole-skin images were analyzed with custom-build IJ1 macros in Fiji ImageJ[39]. Whole RAG mouse skins measured 40.4 cm^2 (RAG15) to 82.5 cm^2 (RAG10) in surface area (**Table S1**). In comparison, C57Bl.6 mouse skins are negligibly thin, measuring on average 0.034 cm (female) and 0.037 cm (male) in thickness[40]. Thus, we dismiss tissue thickness at the macro-scale and treated whole-skin images as two-dimensional surfaces to simplify the analysis. Patch detection was based on grey-scale analysis of the *L. donovani* tdTomato-signal in the isolated red channel with an arbitrary threshold of 70, which consistently gave us good patch detection at all patch sizes. Further, we had to define the minimum size of a patch. Best image resolution allowed for a pixel size of 21.47 µm x 21.47 µm = 461 $µm^2$, which did not

allow to resolve for individual *L. donovani* amastigote, which are 2 – 3 µm in diameter ($r^2 * \pi = 1.5^2 * 3.1416 \approx 7.1\ \mu m^2$). Within a mammalian host, *L. donovani* amastigotes are intracellular; most commonly residing in macrophages[41]. Thus, *L. donovani* amastigote distribution can be describe by their host cell distribution. The cell body shape of phagocytic cells, like macrophages and DCs, is plastic and in tissues like the skin highly irregular, making it difficult to calculate the 2D surface area of such cells. It is easier to calculate the area of rounded cells; luckily, cells like macrophages may occur with rounded cell bodies, too. Assuming that the overall cell surface is the same between a rounded and irregularly shaped macrophage, accepting an average diameter of 25 µm and assuming a flat cell body shape, we can easily calculate an approximate 2D cell area ($r^2 * \pi = 12.5^2 * 3.1416 \approx 491\ \mu m^2$)[42]. This means that a single macrophage would be defined by at least 4 pixels. Using these dimensions, we defined the smallest arguable patch size as 2 x 2 macrophages (at least 9 pixels) in 2D. Thus, $(3 * 21.47\ \mu m)^2 = 4148.65\ \mu m^2$ was set as the smallest possible size to define patches in our stereomicroscopic images. The macro for density-peak detection was adapted from an unpublished, but publicly available protocol from Andrew McNaughton on particle counting in cells (University of Otago, NZ). Further, two standard plugins available for Fiji ImageJ were used; a plugin published by Haeri & Haeri (2015) for nearest neighbor distance (NND) analysis [43] and a plugin published by Ben Tupper to analyze patch clustering[44]. For the latter, a maximum distance of 3.9 mm between patch boarders was chosen. This value was based on the idea that an average sand fly is from proboscis tip to the abdominal posterior about 2 mm long. If we used just <2 mm (1.95 mm) as a radius to mark a circular landing zone for sand flies that landing zone has diameter of 3.9 mm (**Fig. S1D**). Conceptually, any patch reaching into the landing zone may be immediately accessible to a sand fly without moving away from its landing spot. Even if a parasite patches bordered just at the periphery of the

landing zone, parasites from these patches will end up in the blood pool, which has an average diameter of ~1 mm[10].

Confocal image analysis (micro-scale)

The software package, Volocity (V.6; Quorum Tehcnologies), was used for amastigote to epidermis distance measurements. Individual amastigotes were detected by eroding the tdTomato-signal until signal segments coincided with separate sets of YOYO-1 labelled small nuclei and kinetoplasts. The epidermis was demarcated by consolidating all Brilliant Violet 421 signal of Cytokeratin-10 (CK-10) positive areas into a single mass under exclusion of skin appendages. Distances were measured by taking the shortest distance from the centroid of the tdTom amastigotes to the edge of the CK-10 positive band. To collate distance measurements from images from the same RAG mouse and to compare between RAG mice, the measurements required normalization due variations in skin thickness. We estimated the mean thickness of the epidermis, dermis and hypodermis, respectively, for each image by averaging at least three cross measurements in different places for each layer and then adjusted all measurements by the factor of difference between the mean skin layer thickness and the optical skin thickness as measured by Sabino et al. (2016)[40]. While a difference in sex did not significantly affect the macroscale analysis, at the micro-scale, skin shows significant difference between sexes. While epidermal thickness is comparable between male and female C57Bl.6 mice, the dermis of a male C57Bl.6 mouse is ~1.4 times thicker than that of a female. Conversely, the hypodermis of female C57Bl.6 mouse is ~1.84 times thicker than that of a male. This male and female B6.*RAG2*$^{-/-}$ mice are not directly comparable.

The software package, StrataQuest (TissueGnostics), was used to measure *L. donovani* amastigote co-localization in and distribution of Man^{R+} and $CD11c^{+}$ cells in the skin. Amastigotes were detected by segmentation on the tdTomato signal and host nuclei were detected by segmentation on a mask of YOYO-1 signal minus tdTomato signal. Host nuclei were used as a seed and a mask expanded based on Brilliant Violet 421 signal of Man^{R} and Alexa Fluor 647 signal of CD11c to determine cell type. The epidermis mask was demarcated by consolidating Brilliant Violet 421 signal of Man^{R}, Dylight 650 signal of CD11c and YOYO-1 signal areas below the epidermis were excluded by size. Tissue morphology was used to define masks for the dermis and hypodermis. The tissue and cell masks were used to determine the location of the amastigotes.

Code availability

All Fiji ImageJ macros and R scripts used in this study were deposited in on GitHub (All) and are freely available for download.

Statistics

All statistics were conducted in GraphPad PRISM v.8, SPSS v.25[45] or Rstudio v.1.3.959[46] running R v.4.0.2[47]. Prior to test application, parametric test assumption (normality by Shapiro-Wilk Test; equal variance by Brown-Forsythe test; etc) were tested for all data sets. If assumption were not met even after data transformation, appropriate non-parametric tests were selected. In case of the Quadrat test, which is based on chi-square, chi-square had to be replaced by a Fisher's exact test whenever squares of the grid applied to the window of observations had several squares with <5 or at least one square 0 observations, which was the case for all RAG mice. Prior to statistical analysis, all percent datasets were arcsin

transformed. Applied statistical tests are stated throughout the text and in corresponding figure legends. Harvested mouse skins varied considerably in size between RAG mice (40.4 cm^2 – 82.5 cm^2). For comparison and correlation analyses between RAG mice, some data, like total patch area, patch counts, parasite counts were normalized to area / cm^2 and counts / cm^2, respectively. Where data skewness was an issue, we used the median over the mean as a more robust measure of data distribution. Spatial point pattern analysis was performed in Rstudio and is based on the work of Baddeley and co-workers[15]. The following R packages were used for code execution: abind[48], deldir[49], e1701[50], ggpubr[51], goftest[52], graphics[47], grDevices[47], polyclip[53], RandomFields[54], rlist[55], rms.gof[56], scales[57], sp[58], sparr[59], spatstat[15], spatstat.utils[60], stats[47], tensor[61], tidyverse[62] and utils[47]. Each observation in the analysis was verified by at least two different tests. Running multiple test increases confidence in the result as different tests are not always in agreement.

Data availability

The authors declare that the data supporting the findings of the study are available within the article and its Supplementary Information files or are available from the authors upon request.

Acknowledgments

This work was supported by a Wellcome Senior Investigator Award (# WT106203; http://www.wellcome.co.uk) and a MRC Programme Grant (#G1000230; http://www.mrc.ac.uk) to P.M.K. The authors thank Andrew McNaughton from the Confocal / µCT Facility at University of Otago, NZ, for the permission of adapting his protocol and invaluable discussion, Jesus Valenzuela from the VMBU-LMVR at the NIAID/NIH, USA, for encouragement and time made available to complete the manuscript, the Imaging and Cytometry lab and staff, in particular Graeme Park and Jo Marrison, in the Bioscience Technology Facility at the University of York, UK, for use of their equipment and technically knowhow that supported the image acquisition and the staff of the Biological Services Facility at the University of York, UK, for animal husbandry.

Author contributions

J.S.P.D. and P.M.K. designed the study; J.S.P.D., H.A., N.B. and A.R. conducted the experimental studies; J.S.P.D. conducted the spatial point pattern analysis, modelling and all the statistical analysis, which were revised by S.C. and J.W.P.; the manuscript was written by J.S.P.D. and P.M.K. and all authors contributed to the final version; P.M.K. supervised the study and has senior authorship; P.M.K. conceived the study.

Competing financial interest

There are no competing financial interests in relation to this study.

References

1. Ready PD. Biology of Phlebotomine Sand Flies as Vectors of Disease Agents. *Annual Review of Entomology* **58**, 227-250 (2013).

2. Bates PA. Revising Leishmania's life cycle. *Nat Microbiol* **3**, 529-530 (2018).

3. Murray CJL*, et al.* Disability-adjusted life years (DALYs) for 291 diseases and injuries in 21 regions, 1990–2010: a systematic analysis for the Global Burden of Disease Study 2010. *The Lancet* **380**, 2197-2223 (2012).

4. Alvar J*, et al.* Leishmaniasis Worldwide and Global Estimates of Its Incidence. *PLoS ONE* **7**, e35671 (2012).

5. Srivastava S, Shankar P, Mishra J, Singh S. Possibilities and challenges for developing a successful vaccine for leishmaniasis. *Parasites & Vectors* **9**, (2016).

6. Singh N, Kumar M, Singh RK. Leishmaniasis: Current status of available drugs and new potential drug targets. *Asian Pacific Journal of Tropical Medicine* **5**, 485-497 (2012).

7. Ready P. Epidemiology of visceral leishmaniasis. *Clinical Epidemiology* **6**, 147-154 (2014).

8. Miller E*, et al.* Quantifying the Contribution of Hosts with Different Parasite Concentrations to the Transmission of Visceral Leishmaniasis in Ethiopia. *PLoS Neglected Tropical Diseases* **8**, e3288 (2014).

9. Singh OP*, et al.* Xenodiagnosis to evaluate the infectiousness of humans to sandflies in an area endemic for visceral leishmaniasis in Bihar, India: a transmission-dynamics study. *The Lancet Microbe* **2**, e23-e31 (2021).

10. Doehl JSP*, et al.* Skin parasite landscape determines host infectiousness in visceral leishmaniasis. *Nat Commun* **8**, 57 (2017).

11. Valverde JG*, et al.* Increased Transmissibility of Leishmania donovani From the Mammalian Host to Vector Sand Flies After Multiple Exposures to Sand Fly Bites. *J Infect Dis* **215**, 1285-1293 (2017).

12. Laurenti MD*, et al.* Asymptomatic dogs are highly competent to transmit Leishmania (Leishmania) infantum chagasi to the natural vector. *Vet Parasitol* **196**, 296-300 (2013).

13. Molina R*, et al.* Infectivity of Post-Kala-azar Dermal Leishmaniasis Patients to Sand Flies: Revisiting a Proof of Concept in the Context of the Kala-azar Elimination Program in the Indian Subcontinent. *Clin Infect Dis* **65**, 150-153 (2017).

14. Mondal D*, et al.* Quantifying the Infectiousness of Post-Kala-Azar Dermal Leishmaniasis Toward Sand Flies. *Clin Infect Dis* **69**, 251-258 (2019).

15. Baddeley A, Rubak E, Turner R. *Spatial Point Patterns: Methodology and Applications with R*. Chapman and Hall/CRC Press (2015).

16. Iglesias-Guitian JA, Aliaga C, Jarabo A, Gutierrez D. A Biophysically-Based Model of the Optical Properties of Skin Aging. *Computer Graphics Forum* **34**, 45-55 (2015).

17. Dupasquier M, Stoitzner P, van Oudenaren A, Romani N, Leenen PJ. Macrophages and dendritic cells constitute a major subpopulation of cells in the mouse dermis. *J Invest Dermatol* **123**, 876-879 (2004).

18. Lee SH*, et al.* Mannose receptor high, M2 dermal macrophages mediate nonhealing Leishmania major infection in a Th1 immune environment. *J Exp Med* **215**, 357-375 (2018).

19. Merad M, Sathe P, Helft J, Miller J, Mortha A. The dendritic cell lineage: ontogeny and function of dendritic cells and their subsets in the steady state and the inflamed setting. *Annu Rev Immunol* **31**, 563-604 (2013).

20. Mai LT, Smans M, Silva-Barrios S, Fabie A, Stager S. IRF-5 Expression in Myeloid Cells Is Required for Splenomegaly in L. donovani Infected Mice. *Front Immunol* **10**, 3071 (2019).

21. Liu D, Uzonna JE. The early interaction of Leishmania with macrophages and dendritic cells and its influence on the host immune response. *Front Cell Infect Microbiol* **2**, 83 (2012).

22. Wang XN*, et al.* A three-dimensional atlas of human dermal leukocytes, lymphatics, and blood vessels. *J Invest Dermatol* **134**, 965-974 (2014).

23. Tong PL*, et al.* The skin immune atlas: three-dimensional analysis of cutaneous leukocyte subsets by multiphoton microscopy. *J Invest Dermatol* **135**, 84-93 (2015).

24. Barreiro O*, et al.* Pivotal role for skin transendothelial radio-resistant anti-inflammatory macrophages in tissue repair. *Elife* **5**, (2016).

25. Egen JG, Rothfuchs AG, Feng CG, Winter N, Sher A, Germain RN. Macrophage and T cell dynamics during the development and disintegration of mycobacterial granulomas. *Immunity* **28**, 271-284 (2008).

26. Beattie L*, et al.* Dynamic Imaging of Experimental Leishmania donovani-Induced Hepatic Granulomas Detects Kupffer Cell-Restricted Antigen Presentation to Antigen-Specific CD8+ T Cells. *PLoS Pathogens* **6**, e1000805 (2010).

27. Davis JM, Clay H, Lewis JL, Ghori N, Herbomel P, Ramakrishnan L. Real-time visualization of mycobacterium-macrophage interactions leading to initiation of granuloma formation in zebrafish embryos. *Immunity* **17**, 693-702 (2002).

28. Davis JM, Ramakrishnan L. The role of the granuloma in expansion and dissemination of early tuberculous infection. *Cell* **136**, 37-49 (2009).

29. Onfelt B*, et al.* Structurally distinct membrane nanotubes between human macrophages support long-distance vesicular traffic or surfing of bacteria. *J Immunol* **177**, 8476-8483 (2006).

30. Cifuentes-Munoz N, Dutch RE, Cattaneo R. Direct cell-to-cell transmission of respiratory viruses: The fast lanes. *PLoS Pathog* **14**, e1007015 (2018).

31. Bracq L, Xie M, Benichou S, Bouchet J. Mechanisms for Cell-to-Cell Transmission of HIV-1. *Front Immunol* **9**, 260 (2018).

32. Mandell MA, Beverley SM. Continual renewal and replication of persistent Leishmania major parasites in concomitantly immune hosts. *Proc Natl Acad Sci U S A* **114**, E801-E810 (2017).

33. Saunders EC, McConville MJ. Immunometabolism of Leishmania granulomas. *Immunol Cell Biol*, (2020).

34. Carmichael S, Powell B, Hoare T, Walrad P, Pitchford J. Variable bites and dynamic populations; new insights in Leishmania transmission. *bioRxiv*, 285809 (2020).

35. Shaner NC, Campbell RE, Steinbach PA, Giepmans BNG, Palmer AE, Tsien RY. Improved monomeric red, orange and yellow fluorescent proteins derived from Discosoma sp. red fluorescent protein. *Nature Biotechnology* **22**, 1567-1572 (2004).

36. Bezerra-Vasconcelos DR, Melo LM, Albuquerque ÉS, Luciano MCS, Bevilaqua CML. Real-time PCR to assess the Leishmania load in Lutzomyia longipalpis sand flies: Screening of target genes and assessment of quantitative methods. *Experimental Parasitology* **129**, 234-239 (2011).

37. Accart N, Sergi F, Rooke R. Revisiting Fixation and Embedding Techniques for Optimal Detection of Dendritic Cell Subsets in Tissues. *Journal of Histochemistry & Cytochemistry* **62**, 661-671 (2014).

38. Dalton JE*, et al.* Inhibition of receptor tyrosine kinases restores immunocompetence and improves immune-dependent chemotherapy against experimental leishmaniasis in mice. *J Clin Invest* **120**, 1204-1216 (2010).

39. Schindelin J*, et al.* Fiji: an open-source platform for biological-image analysis. *Nat Methods* **9**, 676-682 (2012).

40. Sabino CP*, et al.* The optical properties of mouse skin in the visible and near infrared spectral regions. *J Photochem Photobiol B* **160**, 72-78 (2016).

41. Podinovskaia M, Descoteaux A. Leishmania and the macrophage: a multifaceted interaction. *Future Microbiol* **10**, 111-129 (2015).

42. Guertin DA, Sabatini DM. Cell Size Control. In: *Encyclopedia of Life Sciences* (ed^(eds) (2006).

43. Haeri M, Haeri M. ImageJ Plugin for Analysis of Porous Scaffolds used in Tissue Engineering. *Journal of Open Research Software* **3**, (2015).

44. Tupper B. Graph Plugin and Demo. (ed^(eds) (2010).

45. Corp. I. IBM SPSS Statistics for Windows. (ed^(eds). 25.0. edn. IBM Corp. (2017).

46. RStudio Team. RStudio: Integrated Development for R. (ed^(eds). 1.4 edn. RStudio, PBC. (2020).

47. R Core Team. R: A language and environment for statistical computing. (ed^(eds). 4.0.2. edn. R Foundation for Statistical Computing (2020).

48. Plate T, Heiberger R. abind: Combine Multidimensional Arrays. (ed^(eds). 1.4-5. edn. CRAN (2016).

49. Turner R. deldir: Delaunay Triangulation and Dirichlet (Voronoi) Tessellation. (ed^(eds). 0.1-29. edn. CRAN (2020).

50. Meyer D, Dimitriadou E, Hornik K, Weingessel A, Leisch F. e1071: Misc Functions of the Department of Statistics. (ed^(eds E1071) PTGF). 1.7-4. edn. CRAN (2020).

51. Kassambara A. ggpubr: 'ggplot2' Based Publication Ready Plots. (ed^(eds). 0.4.0. edn. CRAN (2020).

52. Faraway J, Marsaglia G, Marsaglia J, Baddeley A. goftest: Classical Goodness-of-Fit Tests for Univariate Distributions. (ed^(eds). 1.2-2. edn. CRAN (2019).

53. Johnson A, Baddeley A. polyclip: Polygon Clipping. (ed^(eds). 1.10-0. edn. CRAN (2019).

54. Schlather M*, et al.* RandomFields: Simulation and Analysis of Random Fields. (ed^(eds). 3.3.8 edn. CRAN (2020).

55. Ren K. rlist: A Toolbox for Non-Tabular Data Manipulation. (ed^(eds). 0.4.6.1. edn. CRAN (2016).

56. Mukherji S. rms.gof: Root-mean-square goodness-of-fit test for simple null hypothesis. (ed^(eds). 1.0. edn. CRAN (2013).

57. Wickham H, Seidel D. scales: Scale Functions for Visualization. (ed^(eds). 1.1.1. edn. CRAN (2020).

58. Bivand RS, Pebesma E, Gomez-Rubio V. *Applied spatial data analysis with R*. Springer (2013).

59. Davies TM, Marshall JC, Hazelton ML. Tutorial on kernel estimation of continuous spatial and spatiotemporal relative risk. *Stat Med* **37**, 1191-1221 (2018).

60. Baddeley A, Turner R, Rubak E. spatstat.utils: Utility Functions for 'spatstat'. (ed^(eds). 1.17-0. edn. CRAN (2020).

61. Rougier J. tensor: Tensor product of arrays. (ed^(eds). 1.5. edn (2012).

62. Wickham H*, et al.* Welcome to the Tidyverse. *Journal of Open Source Software* **4**, (2019).

Figure Legends

Figure 1 | Evaluation of micro-scale parasite distribution in the skin

(A) Representative tile-scan z-stacked confocal microscope image of a 20 µm thick skin biopsy section of the RAG19 mouse. In cyan Cytokeratin-10 (CK-10; epithelium), in blue YOYO-1 (nuclei and kinetoplasts) and in red tdTomato (*L. donovani* amastigotes). The yellow bar is representative of a sand fly proboscis penetrating into the host skin. (B) Violin plot of normalized *L. donovani* amastigote distance from the epithelium. The number of amastigote distances / RAG mouse measured in *N* = 19 skin section images (RAG19 = 5, RAG20 = 5, RAG21 = 3, RAG22 = 6) are given above each plot. Medians (RAG19 = 100.4 µm [95%CI = 99.84 µm, 101 µm], RAG20 = 59.23 µm [95%CI = 55.93 µm, 61.52 µm], RAG21 = 72.95 µm [95%CI = 71.52 µm, 74.13 µm], RAG22 = 180.7 µm [95%CI = 179.6 µm, 181.9 µm]) and 25% / 75% Percentiles (RAG19 = 78.16 µm / 126 µm, RAG20 = 29.89 µm / 107.3 µm, RAG21 = 36.93 µm / 103.1 µm, RAG22 = 140.6 µm / 233.8 µm) are shown as solid and dotted bars respectively. RAG19-21 were female and RAG22 was a male B6.*RAG2*$^{-/-}$ mouse. The background color code for skin layer thickness: pink = epidermis, yellow = dermis, green = hyodermis, tan = subcutaneous tissue. The average sand fly proboscis skin penetration depth is marked by dot-dashed line. (C – G) Evaluation of amastigote localization in the skin. Each circle is representative for a measurement from one of 21 analyzed skin section images across RAG19-22 (*N*: RAG19 = 5 Sections, RAG20 = 5 Sections, RAG21 = 6 Sections, RAG22 = 5 Sections). (C) Parasite counts / skin layer (Median: Epidermis = 8 [95% CI = 0, 52], Dermis = 2563 [95% CI = 655, 4697], Hypodermis = 253 [95% CI = 75, 379]; Friedman test: *Fr* = 33.06, df = 2, P<0.0001; Dunn's post hoc test: Epi vs Der: P<0.0001, Epi vs Hypo: P=0.0407, Der vs Hypo: P=0.0047). (D) Counts of infected host cell / skin layer (Median: Epidermis = 0 [95% CI = 0, 0], Dermis = 186 [95% CI = 66, 502], Hypodermis = 7 [95% CI =

0, 16]; Friedman test: *Fr* = 29.15, df = 2, P<0.0001; Dunn's post hoc test: Epi vs Der: P<0.0001, Der vs Hypo: P=0.0021). (E) Correlation plot of total parasite counts / skin section against all infected cells / skin section (Spearman r: P<0.0001, r=0.9364, 95% CI: 0.8432 – 0.9749). (F) Percent of detected infected Mannose Receptor positive cells of all infected cells compared to detected infected $CD11c^+$ cells of all detected infected cells (Mean: Man^{R+} = 41.84 [95% CI = 31, 52.69], $CD11c^+$ = 6.96 [95% CI = 4.68, 9.25]; Wilcoxon matched-pairs signed rank test (two-tailed): W = -219, Number of pairs = 21, P<0.0001). (G) Percent of detected infected Mannose Receptor positive cells of all detected Mannose Receptor cells compared to detected infected $CD11c^+$ cells of all detected $CD11^+$ cells (Mean: Man^{R+} = 19.13 [95% CI = 12.57, 25.68], $CD11c^+$ = 9.81 [95% CI = 5.47, 14.14]; Wilcoxon matched-pairs signed rank test (two-tailed): W = -187, Number of pairs = 21, P=0.0005).

Figure 2 | Observational description of the skin parasite landscape

(A) Accumulative qPCR data of estimated parasite loads / biopsy from *N* = 432 biopsies (ø 0.6 cm) of 23 RAG mice (RAG1-8 = 24 biopsies each, RAG9-23 = 16 biopsies each). Median (28794 parasite / biopsy [95% CI = 19618, 36622]) and 25% / 75% Percentiles (6977 / 132604 parasites / biopsy) are shown as solid and dotted bars respectively. (B) Average parasite patch counts / cm^2 of skin for *N* = 23 RAG mice with Mean = 14.52 (SD = 10.91) shown. (C) Accumulative data of the individual area of *N* = 21,904 measured parasite patches from 23 RAG mice. Median (12684 parasite / biopsy [95% CI = 12451, 13033]) and 25% / 75% Percentiles (6284 / 47942 parasites / biopsy) are shown as solid and dotted bars respectively. (D) Representative image of detected patches in the RAG4 mouse skin. (E) Arranges data from *N* = 21,904 individually detected patched from 23 RAG mice arranged by 'A' the ratio of patch counts / size category and by 'B' the contribution of size category to the

overall patched area in the skin. (F) Schematic distribution of skin parasite patches over the skin of RAG4 marked by patch area according to the categories in (E). (G) Accumulative data of mean parasite patch density / patch of *N* = 21,904 individually detected patched from 23 RAG mice. Median (76.29 8-bit grey scale value [95% CI = 76.2, 76.4]) and 25% / 75% Percentiles (73.28 / 81.6 parasites / biopsy) are shown as solid and dotted bars respectively. (H) Representative 8-bit grey-scale image showing the tdTomato light intensity per pixel (RAG4). In magenta are the outlines of detected skin parasite patches. (I) X-Y plots of five 5 mm cross sections through patches measuring tdTomato signal intensity / pixel on grey scale [0 – 255] in the RAG4 skin image. The arbitrary cut-off for patch detection set at 70 is marked in these graphs with black dashed line. (J) Image of the RAG4 image indicating where cross sections through parasite patches were made.

Figure 3 | Correlation plots for skin parasite patch characterization

(A) Correlation plot of total parasite patched skin by area (μm^2) against the size of the biggest parasite patch detected in each of the 23 RAG mice (both on a log-scale; Spearman r: two-tailed p<0.0001, r=0.9792, 95% CI=0.9496 – 0.9915). (B) Correlation plot of *N* = 21,904 skin parasite patches by area (μm^2) from 23 RAG mice (on a log-scale) against their respective mean pixel density on a 8-bit grey scale (Spearman r: two-tailed P<0.0001, r=0.6554, 95% CI=0.6476 – 0.6631). (C) Correlation plot of *N* = 21,904 skin parasite patches by area (μm^2) from 23 RAG mice against the number of high-density peaks per individual patch (both on a log-scale; Spearman r: two-tailed P<0.0001, r=0.3831, 95% CI=0.3714 – 0.3947). (D) Correlation plot of total parasite patched skin by area (μm^2) normalized to 1 cm^2 of skin against parasite burden / cm^2 for each of the 23 RAG mice (both on a log-scale; Spearman r: two-tailed P<0.0001, r=0.7589, 95% CI=0.4948 – 0.8947). (E) Correlation plot of total skin

parasite patch counts normalized to 1 cm^2 of skin against mean parasite burden per punch biopsy for each of the 23 RAG mice (on a log-scale; Spearman r two-tailed P=0.0021, r=0.5741, 95% CI=0.1997 – 0.8022). (F) Correlation plot of total parasite patched skin by area (μm^2) normalized to 1 cm^2 of skin (on a log-scale) against total skin parasite patch counts normalized to 1 cm^2 of skin for each of the 23 RAG mice (Spearman r: two-tailed P<0.0001, r=0.8656, 95% CI: 0.6984 – 0.9432). (G) Correlation plot of the median patch area (μm^2) against total skin parasite patch counts for each of the 23 RAG mice (Spearman r: two-tailed P=0.006, r=-0.5148, 95% CI=-0.7701 to -0.1175). (H) Correlation plot of total parasite patched skin by area (μm^2; on a log-scale) against the skewness of parasite patch area data for each of the 23 RAG mice (two-tailed Spearman r: two-tailed P<0.0001, r=0.8686, 95% CI=0.7044 – 0.9445). (I) Correlation plot of total parasite patched skin by area (μm^2; on a log-scale) against the test statistic that infers skewness to the population for each of the 23 RAG mice (Spearman r: two-tailed P<0.0001, r=0.9279, 95% CI=0.8311 – 0.9701).

Figure 4 | Spatial point pattern analysis of skin parasite patch distribution

All graphs are examples for spatial point pattern analysis based on the RAG4 data. (A) Spatial point pattern of skin parasite patches based on center of mass of each detected patch without respective marks. (B) Spatial point pattern of skin parasite patches based on center of mass of each detected patch with respective patch area mark. (C) Patch intensity representation of skin parasite patches based on center of mass of each detected patch without respective marks. (D) Patch intensity representation of skin parasite patches based on center of mass of each detected patch with respective patch area mark. (E) Representation of a cluster analysis output linking all patches whose patch boarders are ≤3.9 mm into a network. (F) Graphical representation of the isotropy test showing the theoretical

Poisson process (red dotted line), the RAG4 data (black solid line) and the global envelops (grey). (G) Graphical representation of correlation-stationary test based on a locally scaled K-function. (H) Scaled L-function showing the theoretical Poisson process (red dotted line), the RAG4 data (black solid line) and the global envelopes (grey). (I) Pair correlation function the theoretical Poisson process (red dotted line), the RAG4 data (black solid line). (K) Data points independence test based on K-function of the data residuals, showing the theoretical Poisson process (red dotted line), the RAG4 data (black solid line) and the upper (green) and lower limits (blue) of the confidence intervals of the theoretical Poisson process.

Figure 5 | Basic model evaluation of skin parasite patch distribution

(A) Scaled L-function showing the theoretical Poisson process (red dotted line), the RAG4 predicted model data (black solid line) and the global envelopes (grey). (B) Four model simulations based on the Matérn cluster process for RAG4.

Figure 6 | Proposed mechanism of skin parasite patch dispersal

(A) After an initial *Leishmania* amastigote seeding event in the host skin by arrival of infected host cells presumably from circulation, uninfected phagocytic cells in skin are attracted to the infected cells to form a type of innate granuloma. (B) Attracted naïve phagocytic cells are then gradually infected in the innate granuloma, forming a parasite patch. (C) As parasite patches keep growing, they seed new patch within a radius ‘r’ around themselves, potentially by escape of infected host cells or through direct transfer. (D) This process then repeats itself, forming a self-propagating network of parasite patch clusters.

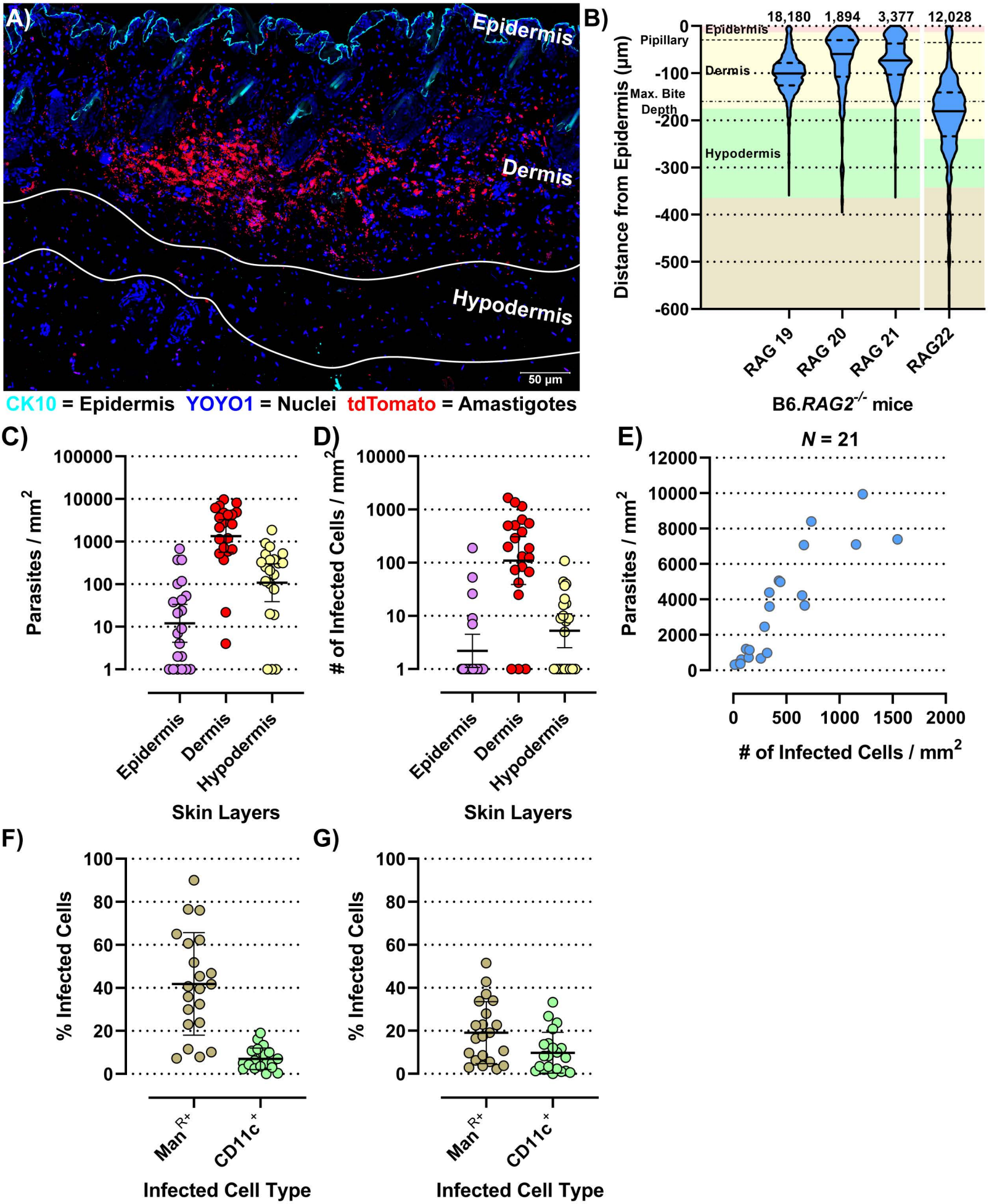
A)
Epidermis
Dermis
Hypodermis
50 µm
CK10 = Epidermis YOYO1 = Nuclei tdTomato = Amastigotes
B)
18,180
1,894
3,377
12,028
Epidermis
Pipillary
Dermis
Max. Bite Depth
Hypodermis
Distance from Epidermis (µm)
0
-100
-200
-300
-400
-500
-600
RAG 19
RAG 20
RAG 21
RAG22
B6.RAG2-/- mice
C)
Parasites / mm2
100000
10000
1000
100
10
1
Epidermis
Dermis
Hypodermis
Skin Layers
D)
# of Infected Cells / mm2
10000
1000
100
10
1
Epidermis
Dermis
Hypodermis
Skin Layers
E)
N = 21
Parasites / mm2
12000
10000
8000
6000
4000
2000
0
0
500
1000
1500
2000
# of Infected Cells / mm2
F)
% Infected Cells
100
80
60
40
20
0
ManR+
CD11c+
Infected Cell Type
G)
% Infected Cells
100
80
60
40
20
0
ManR+
CD11c+
Infected Cell Type

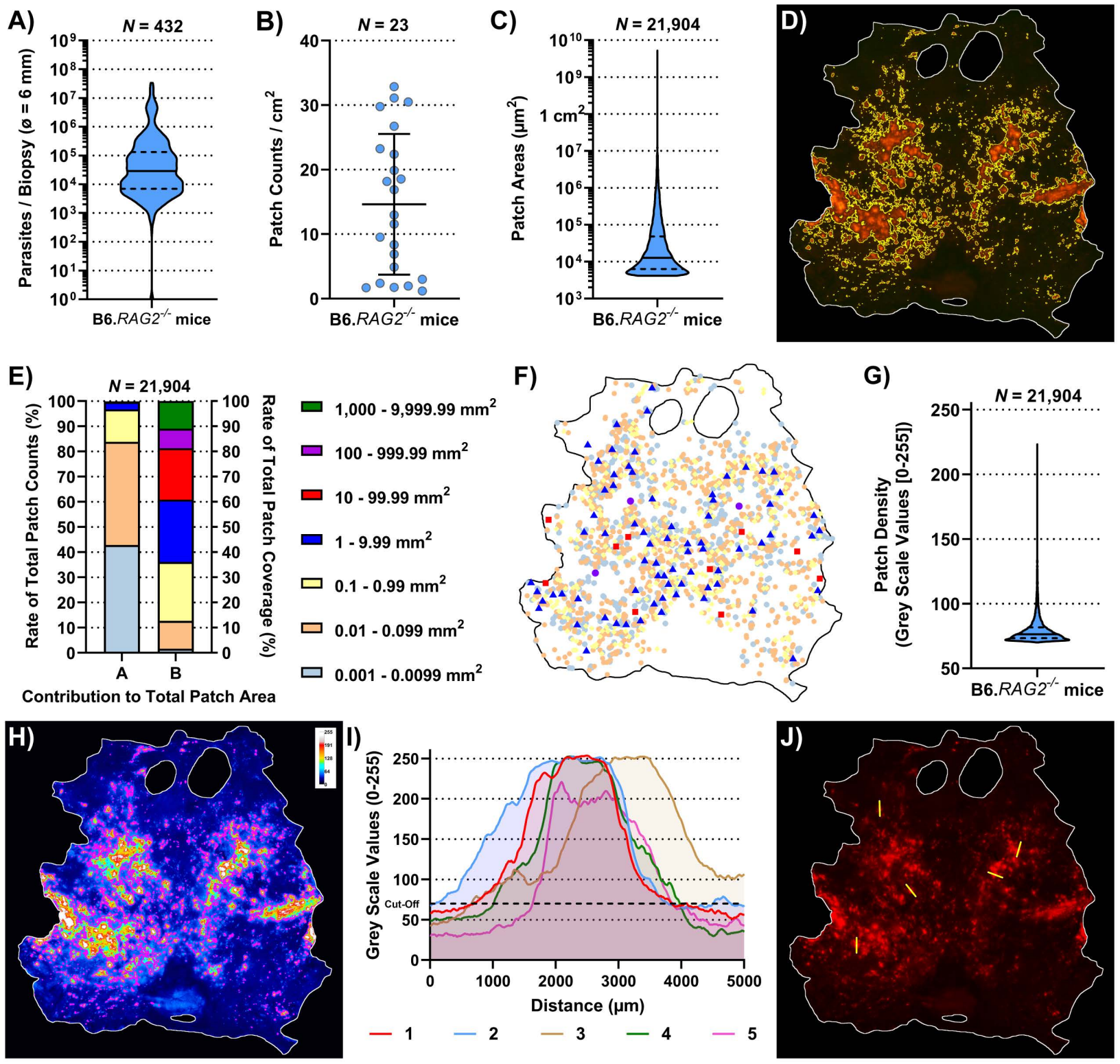
A)
N = 432
Parasites / Biopsy (ø = 6 mm)
B6.RAG2-/- mice
B)
N = 23
Patch Counts / cm2
B6.RAG2-/- mice
C)
N = 21,904
Patch Areas (µm2)
1 cm2
B6.RAG2-/- mice
D)
E)
N = 21,904
Rate of Total Patch Counts (%)
Rate of Total Patch Coverage (%)
Contribution to Total Patch Area
1,000 - 9,999.99 mm2
100 - 999.99 mm2
10 - 99.99 mm2
1 - 9.99 mm2
0.1 - 0.99 mm2
0.01 - 0.099 mm2
0.001 - 0.0099 mm2
F)
G)
N = 21,904
Patch Density (Grey Scale Values [0-255])
B6.RAG2-/- mice
H)
I)
Grey Scale Values (0-255)
Cut-Off
Distance (µm)
1
2
3
4
5
J)

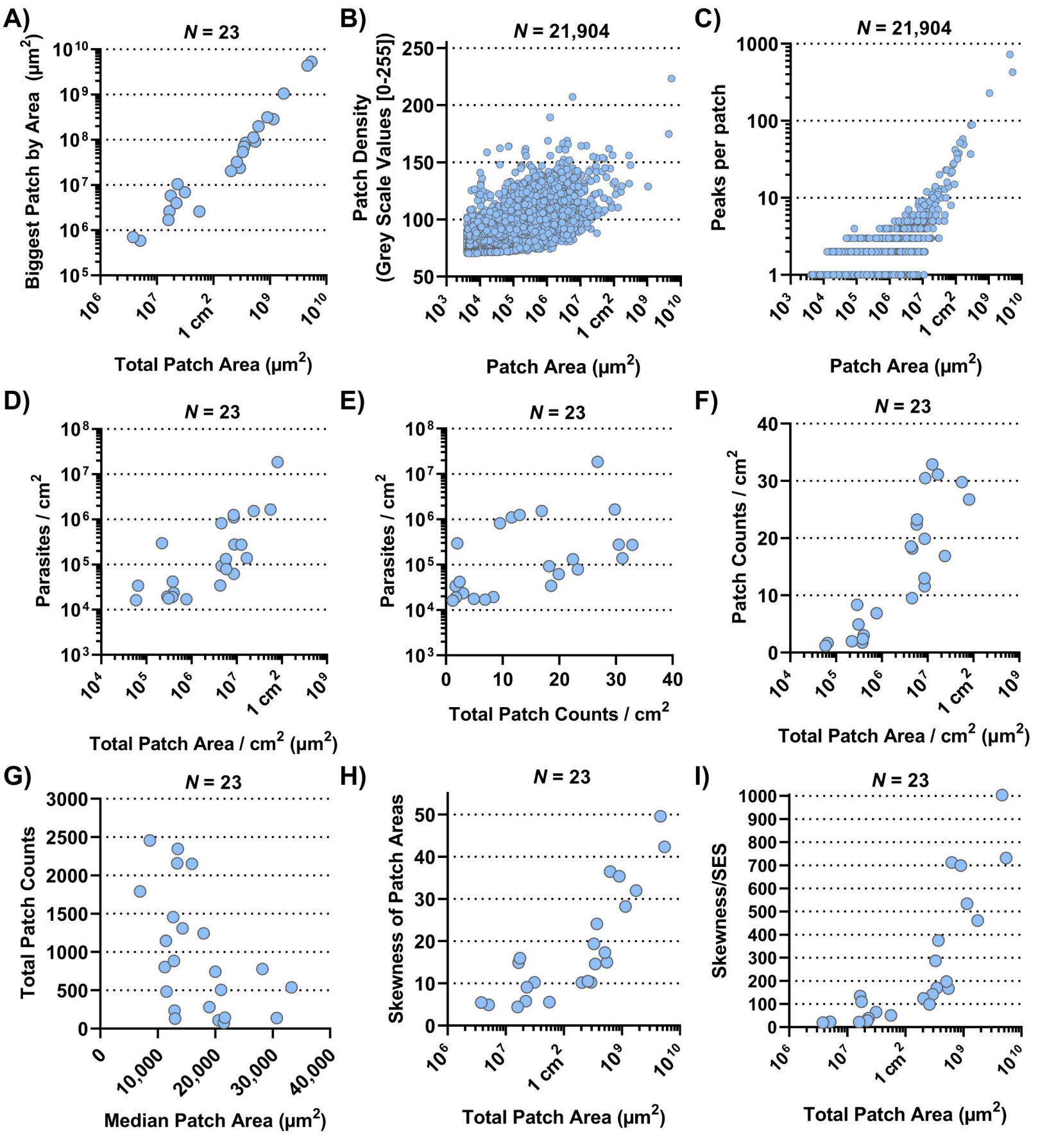
A)
N = 23
Biggest Patch by Area (μm²)
Total Patch Area (μm²)
B)
N = 21,904
Patch Density (Grey Scale Values [0-255])
Patch Area (μm²)
C)
N = 21,904
Peaks per patch
Patch Area (μm²)
D)
N = 23
Parasites / cm²
Total Patch Area / cm² (μm²)
E)
N = 23
Parasites / cm²
Total Patch Counts / cm²
F)
N = 23
Patch Counts / cm²
Total Patch Area / cm² (μm²)
G)
N = 23
Total Patch Counts
Median Patch Area (μm²)
H)
N = 23
Skewness of Patch Areas
Total Patch Area (μm²)
I)
N = 23
Skewness/SES
Total Patch Area (μm²)

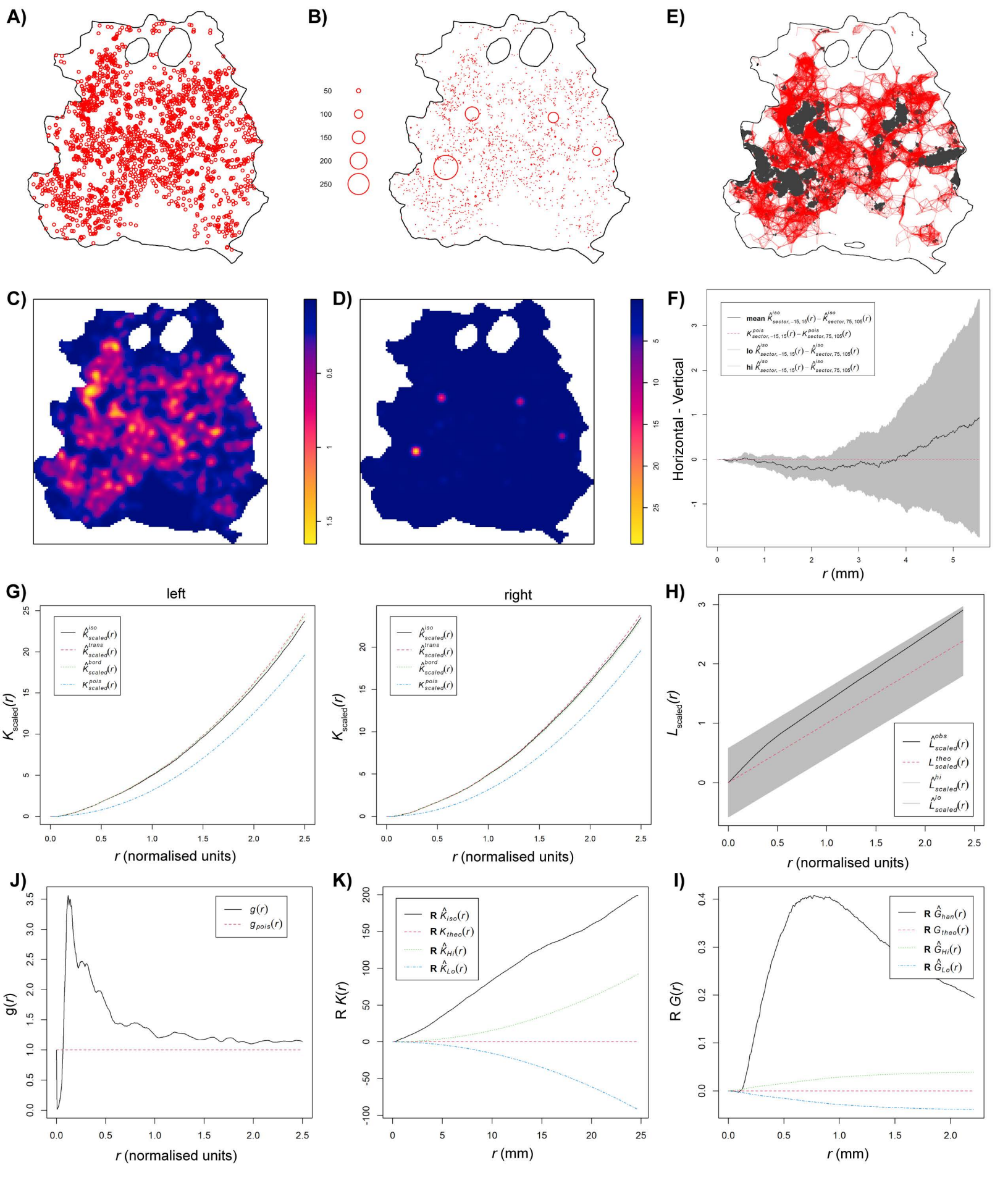
A)
B)
50
100
150
200
250
E)
C)
D)
F)
mean $\hat{K}^{iso}_{sector,-15,15}(r) - \hat{K}^{iso}_{sector,75,105}(r)$
$K^{pois}_{sector,-15,15}(r) - K^{pois}_{sector,75,105}(r)$
lo $\hat{K}^{iso}_{sector,-15,15}(r) - \hat{K}^{iso}_{sector,75,105}(r)$
hi $\hat{K}^{iso}_{sector,-15,15}(r) - \hat{K}^{iso}_{sector,75,105}(r)$
Horizontal - Vertical
r (mm)
G)
left
right
$\hat{K}^{iso}_{scaled}(r)$
$\hat{K}^{trans}_{scaled}(r)$
$\hat{K}^{bord}_{scaled}(r)$
$K^{pois}_{scaled}(r)$
$K_{scaled}(r)$
r (normalised units)
H)
$\hat{L}^{obs}_{scaled}(r)$
$L^{theo}_{scaled}(r)$
$\hat{L}^{hi}_{scaled}(r)$
$\hat{L}^{lo}_{scaled}(r)$
$L_{scaled}(r)$
r (normalised units)
J)
$g(r)$
$g_{pois}(r)$
g(r)
r (normalised units)
K)
R $\hat{K}_{iso}(r)$
R $K_{theo}(r)$
R $\hat{K}_{Hi}(r)$
R $\hat{K}_{Lo}(r)$
R K(r)
r (mm)
I)
R $\hat{G}_{han}(r)$
R $G_{theo}(r)$
R $\hat{G}_{Hi}(r)$
R $\hat{G}_{Lo}(r)$
R G(r)
r (mm)

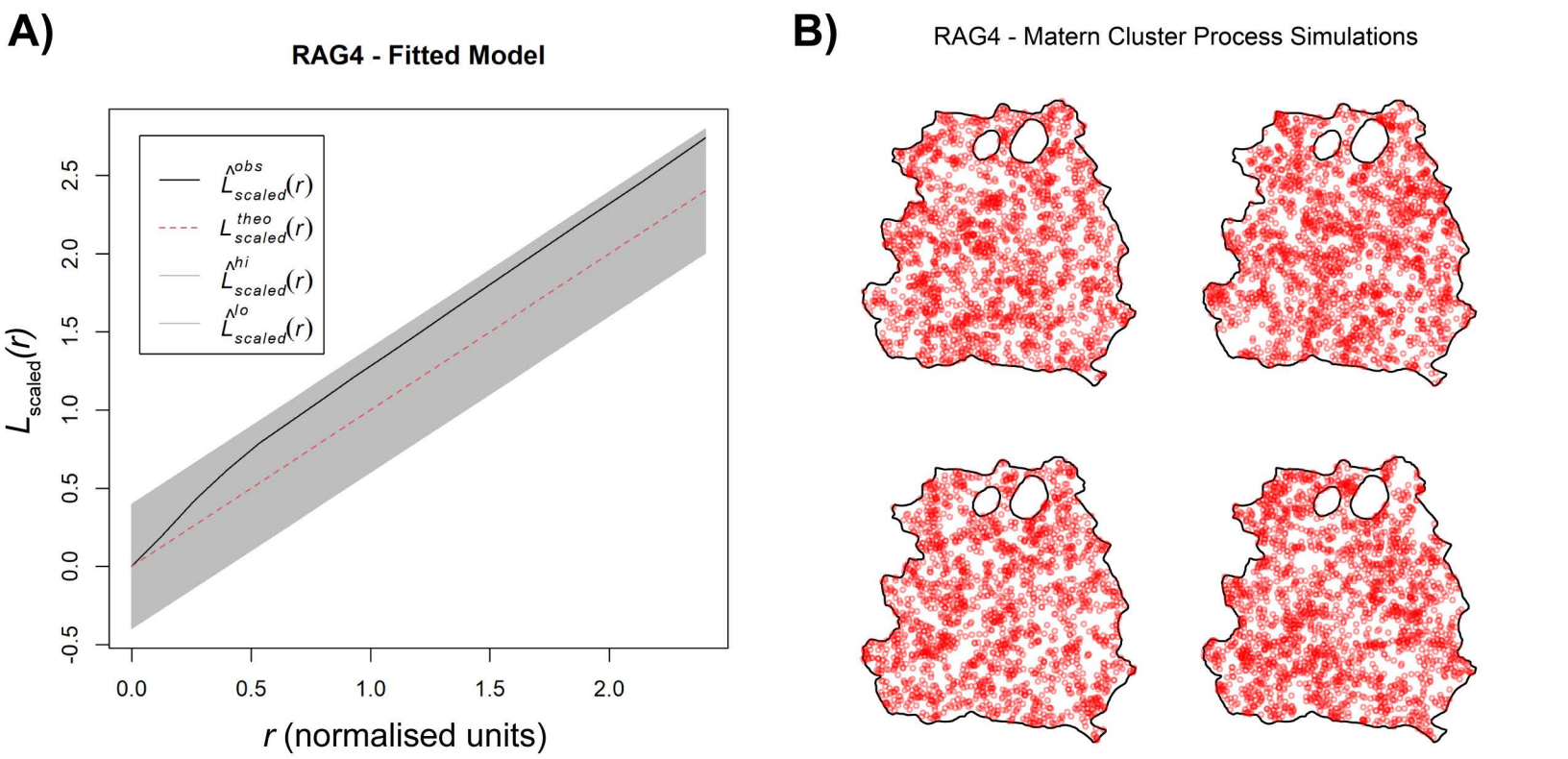
A)
RAG4 - Fitted Model
$\hat{L}^{obs}_{scaled}(r)$
$L^{theo}_{scaled}(r)$
$\hat{L}^{hi}_{scaled}(r)$
$\hat{L}^{lo}_{scaled}(r)$
$L_{scaled}(r)$
-0.5
0.0
0.5
1.0
1.5
2.0
2.5
0.0
0.5
1.0
1.5
2.0
r (normalised units)
B)
RAG4 - Matern Cluster Process Simulations

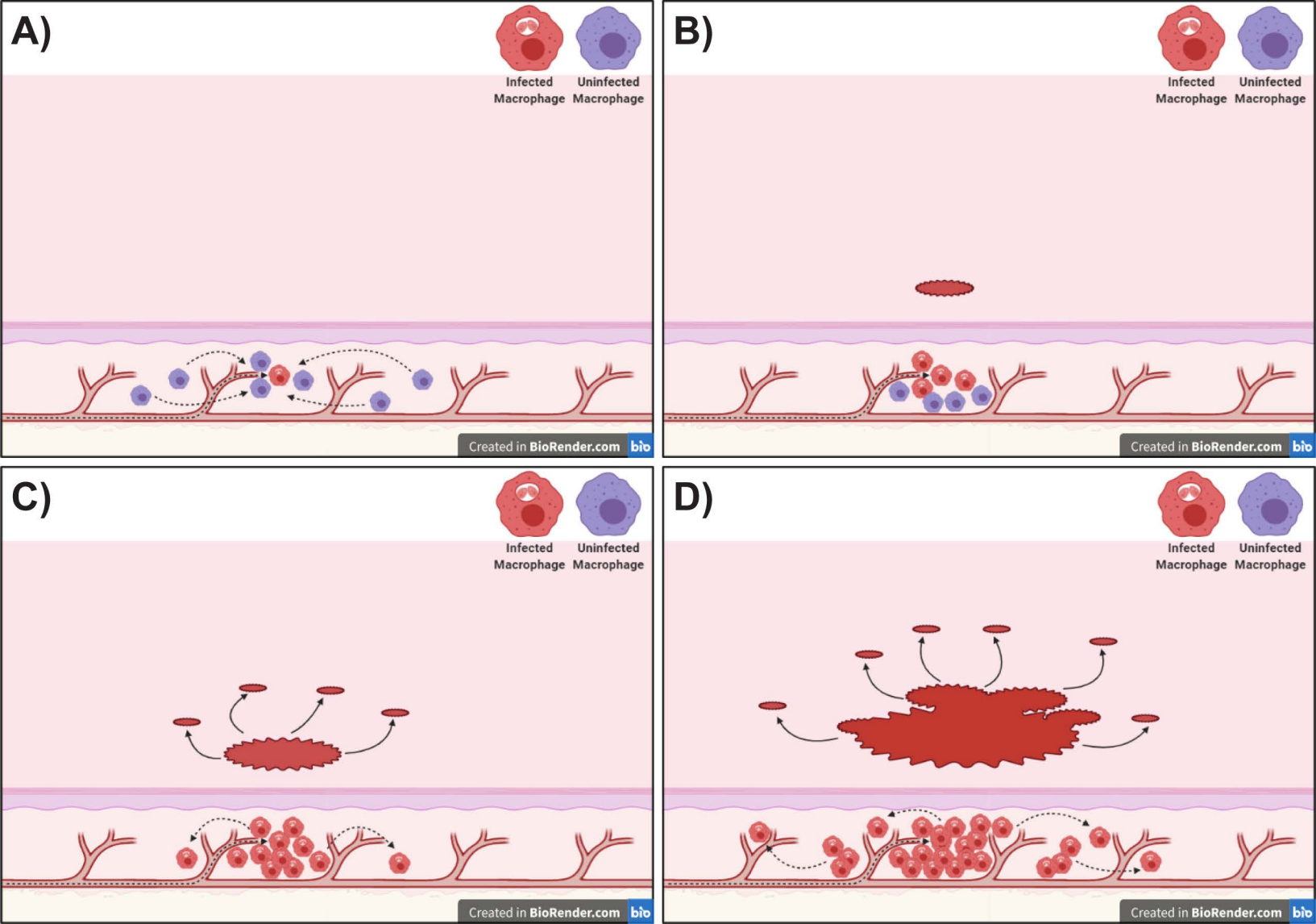
A)
Infected Macrophage
Uninfected Macrophage
Created in BioRender.com
B)
Infected Macrophage
Uninfected Macrophage
Created in BioRender.com
C)
Infected Macrophage
Uninfected Macrophage
Created in BioRender.com
D)
Infected Macrophage
Uninfected Macrophage
Created in BioRender.com